Article

Not peer-reviewed version

Photonic-Chemical Coupling in Confined Catalytic Nanocavities for Selective Energy Conversion

Pietro Perlo *, Marco Dalmasso, Luca Belforte, Vito Lambertini, Nello Li Pira

Posted Date: 5 May 2026

doi: 10.20944/preprints202605.0211.v1

Keywords: confined combustion; anodic porous alumina; nanocavities; photonic-chemical coupling; selective energy conversion; thermophotovoltaics; thermoelectrics

 doi:10.20944/preprints202605.0211.v1

Article

Photonic-Chemical Coupling in Confined Catalytic Nanocavities for Selective Energy Conversion

Pietro Perlo [1,*], Marco Dalmasso [1], Luca Belforte [2], Vito Lambertini [2] and Nello Li Pira [2]

[1] Interactive Fully Electrical VehicleS (IFEVS), Strada Carignano 50, 10040 La Loggia, Italy

[2] Centro Ricerche Fiat, Strada Torino 50, 10043 Orbassano, Italy

* Correspondence: pietro.perlo@ifevs.com

Abstract

Selective energy conversion in confined catalytic nanocavities is examined through a coupled reactive-photonic framework rather than only as a microscale flame-stability problem. The experimental basis combines visible/NIR spectral measurements from Pt-coated anodic porous alumina (APA) nanocavities with a smooth zirconia reference, together with structural information on ordered nanocavity platforms. Within the measured window, the Pt-coated APA spectrum departs more strongly from the corresponding grey-body fit than the zirconia reference, providing direct experimental indication that confinement alters radiative behaviour at accessible wavelengths. We interpret this divergence through a photonic-chemical coupling framework in which high-aspect-ratio cavities reduce access to free-space long-wavelength radiative escape while increasing wall-coupled relaxation and catalytic-interface interaction. A converged FDTD benchmark at the dominant CO_2-4.3 μm band (Purcell factor $F_p \approx 1.26$) shows moderate total LDOS enhancement while aperture flux is suppressed by more than six orders of magnitude relative to total radiated power. This indicates that the cavity redirects the emitted energy into wall-coupled channels rather than allowing free-space axial emission. The result is not a full mid-IR device demonstration, but a mechanistically grounded, computationally supported case that confined combustion in Pt-coated APA can operate as an integrated selective emitter and wall-coupled heat-redistribution architecture relevant to thermophotovoltaic and hybrid TPV/TEG energy conversion.

Keywords: confined combustion; anodic porous alumina; nanocavities; photonic-chemical coupling; selective energy conversion; thermophotovoltaics; thermoelectrics

1. Introduction

Portable and distributed power systems continue to motivate interest in small-scale combustion because liquid and gaseous fuels remain far denser energy carriers than current electrochemical storage. For that reason, small-scale combustion remains attractive not only as a heat source but also as a potential front end for selective energy conversion. Yet classical microcombustion is difficult: as characteristic size decreases, the surface-to-volume ratio rises, flame-wall interaction becomes dominant, quenching becomes easier, and the system can lose more heat than it can productively convert [13–16]. Most of the field has therefore concentrated on heat recirculation, porous burners, catalytic stabilization, and ignition/extinction limits [13–16].

Relative to heat-recirculating burners, porous burners and catalytic microcombustors, the Pt-coated APA platform is distinctive because the confinement length scale is brought into the submicrometric regime where geometry can influence both reaction environment and radiative phase space [13–16]. The wall is therefore not only a heat sink or catalyst support; it becomes part of the spectral-selection architecture. In that sense the present system occupies a geometric LDOS-control regime under realistic combustion conditions: more structured than classical porous catalysts, but not in the vibrational strong-coupling regime of idealized cavity-chemistry experiments [20,21,29,37,38].

 doi:10.20944/preprints202605.0211.v1

In parallel, a separate scientific tradition has shown that emission is not an intrinsic property of the emitter alone but depends strongly on the electromagnetic environment. Bykov first framed spontaneous emission in periodic structures, and the later work of Yablonovitch and John made explicit that structured optical media can inhibit, localize or redirect radiation by changing the density of accessible photonic states [1–3]. Microcavities and related photonic architectures therefore offer a way to reformulate small-scale combustion: not only as a fluid-chemical process, but also as a problem of mode selection, radiative transport and spectral control [4,20,21,24].

A deliberately bio-inspired lens is especially appropriate for this problem. In biology, confinement is not an exception; it is the operating principle of energy conversion. Membrane-defined compartments make chemiosmotic ATP production possible, plastid architecture improves photosynthetic efficiency, and firefly lanterns combine oxygen delivery, chemical activation and optical extraction in the same structured organ [5–10,33]. While classical microcombustion often treats the wall as a passive heat sink or catalytic site, biological organelles show that compartmentalisation is an active thermodynamic variable that enforces transport directionality and energy selectivity.

By adopting this active-compartment view, experimental data from ordered nanocavities and Pt-coated anodic porous alumina are interpreted here as evidence for a broader concept: confined combustion as engineered compartmentalisation of a reactive energy source and as a photonic-chemical gate for selective energy conversion pathways. Visible/NIR spectroscopy provides direct experimental indication that Pt-coated APA nanocavities depart significantly from grey-body behaviour within the measured window. For the critical 2–15 μm mid-infrared region where H_2O and CO_2 rovibrational bands emit, propagating transverse modes are placed in a severe cutoff regime (see Section 3). The net effect on free-space mid-IR escape, the quantity that matters for a downstream energy converter, is a strong reduction, even if the total LDOS is moderately enhanced. This refined mechanism is examined quantitatively in Section 5. The combination of experimental indication at accessible wavelengths and targeted full-wave simulations provides a robust foundation for the proposed photonic-chemical coupling mechanism.

The net effect on *free-space mid-IR escape*, the quantity that matters for a downstream energy converter, is a dramatic reduction, even if the total LDOS is not suppressed. This refined mechanism is tested quantitatively through converged FDTD simulations.

That broader interpretation is consistent with the modern literature on chemistry under confinement. Across nanopores, catalytic nanoreactors and confined fluids, confinement is no longer viewed as a passive geometric boundary; it can modify local concentration fields, adsorption strength, molecular orientation, transport kinetics, intermediate stability, phase behaviour and reaction selectivity [29–31]. In reaction-theory terms, confinement can reshape the effective reaction coordinate by perturbing translational freedom, collision orientation, adsorption lifetimes, solvent or field stabilisation, and the branching between radiative and non-radiative relaxation [29–31,37,38]. The hydrogen-oxygen-to-water system illustrates why textbook bulk stoichiometry is insufficient. The net reaction $2\,H_2 + O_2 \rightarrow 2\,H_2O$ hides a manifold of adsorbed and short-lived states—O, *OH*, OOH, *H_2O*, and hot rovibrational products whose populations depend on local geometry and interfaces. Under interfacial confinement, water formation can proceed through alternative pathways and altered intermediate stabilisation relative to the bare-surface route [32]. For the present Pt-coated cavities, the claim is therefore not simply that combustion is miniaturised, but that the chemistry and the available electromagnetic relaxation channels are jointly conditioned by confinement.

2. Why Biology Is an Appropriate Model

Biological systems show that confinement does much more than reduce size. It creates functional asymmetry. Compartments separate incompatible chemistries, enforce transport directionality, preserve useful gradients and increase selectivity by controlling where energy is allowed to flow [5–7]. In mitochondria and chloroplasts, spatial organisation is inseparable from energetic performance. Reaction and transport pathways are encoded in geometry.

 doi:10.20944/preprints202605.0211.v1

The firefly lantern provides an especially relevant analogy because it links chemistry, mass transfer and optics. Nitric-oxide-mediated oxygen gating controls when oxygen reaches photocytes, and cuticular optical nanostructures improve extraction of useful visible light [8–10]. This is strikingly close to the engineering objective of confined combustion: localise the reactive zone, regulate access to oxidant and surfaces, and favour useful emission or heat transfer pathways over dissipative broadband loss.

From an engineering standpoint, the lesson is direct. A confined combustor should not be optimised only for adiabatic flame temperature or complete conversion. It should also be optimised for spectral usefulness, directional transport, wall coupling and compatibility with downstream energy-conversion elements. The bio-inspired implication is therefore methodological: the reactor should be treated as an active compartment with multiple coupled selection functions rather than as a miniature version of a conventional flame tube.

3. Nanocavity Interaction and Redistribution of Rovibrational Emission

3.1. Theoretical Framework

The core physical claim of this paper is that nanocavities modify not only the local temperature field but also the radiative phase space available to excited combustion products. A photonic-chemical coupling framework is therefore adopted: nanocavities modify the local photonic density of states (LDOS), which in turn changes the branching between radiative decay, wall-assisted quenching, phonon generation and surface-mediated chemical relaxation. A useful starting point is the familiar cavity-optics expression

$$S(\omega,T)=\rho(\omega)W(\omega,T),$$
$$W(\omega,T)=\frac{\hbar\omega}{\exp\left(\hbar\omega/k_BT\right)-1},$$
$$S_p(\omega,T)=\rho_v(\omega)VW(\omega,T),\rho_v(\omega)=\frac{\omega^2}{\pi^2c^3},$$
$$G(\omega,T)=\frac{S(\omega,T)}{S_p(\omega,T)}.$$

Here $\varrho(\omega)$ is the local photonic density of states, W(ω,T) the Planck mean energy of the mode, and $\varrho_{v(\omega)}$ the free-space modal density per unit volume. Within this framework G(ω,T) < 1 denotes inhibited radiative output and G(ω,T) > 1 denotes enhancement. The geometric requirement for strong modification is that the pore diameter be of the same order as the wavelength inside the medium, d ~ λ/n, while the cavity remains high aspect ratio (h/d ≫ 1), so that the pore behaves as a reflective quasi-waveguide rather than as a shallow rough surface [4].

$$k_{\mathrm{rad}}^{\mathrm{cav}}(\omega)=F_p(\omega)k_{\mathrm{rad}}^{0}(\omega),$$
$$k_{\mathrm{tot}}=k_{\mathrm{rad}}^{\mathrm{cav}}+k_{\mathrm{wall}}+k_{\mathrm{nr}}+k_{\mathrm{chem}},$$
$$\Phi_{\mathrm{rad}}(\omega)=\frac{k_{\mathrm{rad}}^{\mathrm{cav}}(\omega)}{k_{\mathrm{tot}}}.$$

Here $F_{p(\omega)}$ is the cavity-induced radiative factor (Purcell factor), k_{wall} collects wall-assisted absorption and quenching processes, k_{nr} non-radiative molecular relaxation, and k_{chem} chemically coupled dissipation or reactivity-assisted relaxation at the catalytic interface. In the present framework, the key distinction is between total LDOS and free-space escape. The cavity-induced factor $F_p(\omega)$ can be greater than 1 because evanescent, surface, and cavity-assisted channels increase the local optical density of states, while the fraction of power reaching free space is simultaneously reduced by wall-coupled dissipation and cutoff-limited axial propagation.

The operationally relevant quantity for energy conversion is not the total LDOS but the fraction of power that escapes into free space. The cavity can enhance the total emission rate while simultaneously redirecting most of that energy into wall-coupled channels.

 doi:10.20944/preprints202605.0211.v1

3.2. Waveguide Cutoff as a Guide for Free-Space Escape

For reflective cylindrical cavities, the resonance and cutoff positions follow from the zeros of the Bessel functions [4]. Using the cylindrical waveguide approximation, the first characteristic wavelengths are approximately $\lambda_{parallel} \approx 1.31$ D and $\lambda_{perp} \approx 1.71$ D, where D is the cavity diameter [4]. For D = 300 nm these values are about 393 nm and 513 nm; for D = 400 nm they are about 524 nm and 684 nm. In the idealised limit, *propagating transverse modes* are strongly disadvantaged for wavelengths > λ_{perp}. All important rovibrational bands of H_2O and CO_2 lie at 2–15 μm, far above this cutoff. Hence, any free-space wave launched along the pore axis cannot propagate; it becomes evanescent and is largely absorbed by the metallic walls or converted into surface modes.

Crucial distinction: This cutoff argument does **not** predict the total LDOS, it only describes the fate of *propagating* modes in an infinite, perfectly conducting waveguide. In a real, finite, open metallic cavity, the total LDOS includes contributions from evanescent fields, lossy surface-plasmon-polariton modes and longitudinal Fabry-Perot resonances. These contributions can lead to an *enhancement* of the total LDOS ($F_p > 1$) even while the *free-space axial escape* is strongly suppressed. This refined picture is confirmed by the full-wave FDTD simulations in Section 5.

3.3. Engineering Relevance

The key quantity for a downstream thermophotovoltaic (TPV) cell or a thermoelectric (TEG) module is the power that escapes the cavity and propagates to the converter in free space. If that power is reduced, the cavity is effectively acting as a selective emitter that redirects energy into the solid matrix (wall heating). The suppressed portion need not be lost: it becomes available as conductive heat for a cascaded TEG. This is the essence of the proposed photonic-chemical coupling.

Figure 1 summarises the proposed photonic-chemical coupling mechanism. Shorter-wave channels near the cavity-supported range can still outcouple, whereas the long-wave rovibrational channels of the hot products encounter a strongly reduced probability of free-space axial escape. The likely consequence is a redistribution of energy toward the walls and the surrounding solid rather than unrestricted infrared escape.

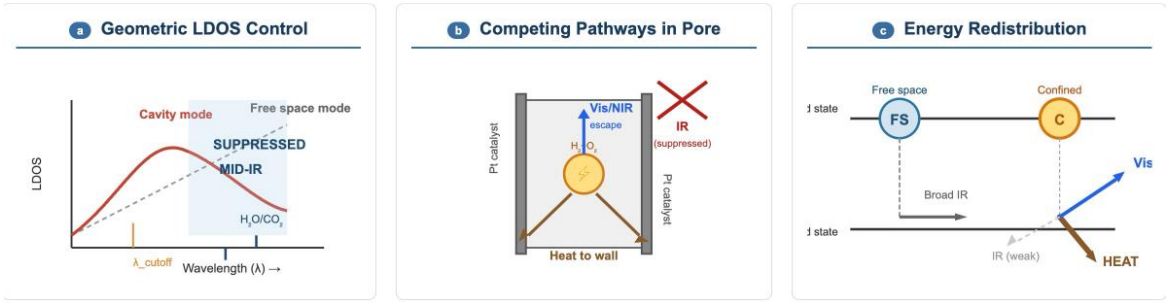

Figure 1. Photonic-chemical coupling mechanism. a, Cavity geometry modifies LDOS: "Free space mode" (dashed line) vs "Cavity mode" (red curve). Mid-IR region where H_2O and CO_2 emit is highlighted. b, Within a pore: IR emission largely redirected (red X on axial escape), Vis/NIR escape possible vertically upward (blue arrow), heat dissipation to Pt walls (brown arrows). c, Energy redistribution: Confined molecule (C) redirects energy from broadband IR toward heat (dominant) and visible channels, compared to free space (FS).

Table 1. Idealised waveguide cutoff parameters and their implication for free-space propagation.

Platform	D (nm)	$\lambda_{parallel}$ ≈1.31D (nm)	λ_{perp} ≈1.71D (nm)	Implication for mid-IR free-space escape
Metallic cavity array	400	524	684	TE_{11} cutoff at 684 nm: all mid-IR propagating modes are cut off → free-space axial emission strongly suppressed.
Pt-coated APA pore	300	393	513	Even stronger suppression of axial propagation; wall-coupled energy transfer favoured.

 doi:10.20944/preprints202605.0211.v1

Note: This table describes the fate of propagating transverse modes; the total LDOS may still be enhanced due to evanescent and surface modes (see Section 5).

4. Experimental Basis and Quantitative Indicators

4.1. Experimental Platform

The experimental basis combines two complementary elements: (i) direct visible/NIR spectral measurements from Pt-coated APA nanocavities compared to a smooth zirconia reference, and (ii) a well-established geometric principle governing wave propagation in subwavelength cavities. The experimental dataset from the authors' archive contains two nanocavity routes: ion-beam-defined metallic cavities with nominal diameter D ≈ 400 nm and depth ≈ 20 μm, and self-ordered anodic porous alumina with pore diameter D ≈ 300 nm and interpore spacing ≈ 430 nm, subsequently used as the Pt-coated combustion platform. The structural parameters (D ≈ 300 nm, interpore spacing a ≈ 430 nm, depth ≈ 20 μm) directly define the representative geometry used in the FDTD simulations of Section 5.

The visible/NIR data in Figure 2 provide experimental indication that the Pt-coated nanocavity system already exhibits significant deviation from grey-body behaviour within the measured window, a deviation that is absent for the smooth zirconia reference surface. This establishes that confinement fundamentally alters the radiative properties of the system even at wavelengths near the cavity cutoff.

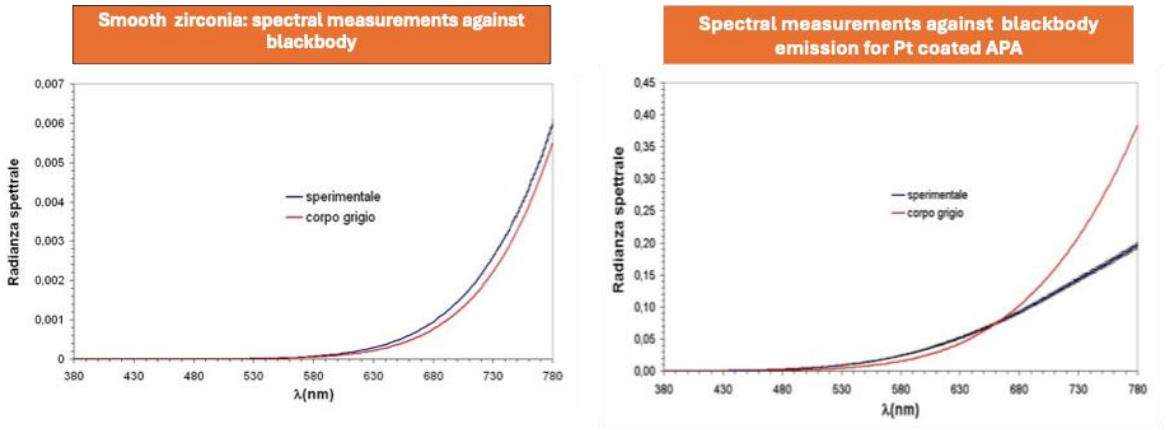

Figure 2. Experimental visible/NIR spectral comparison against grey-body fits.

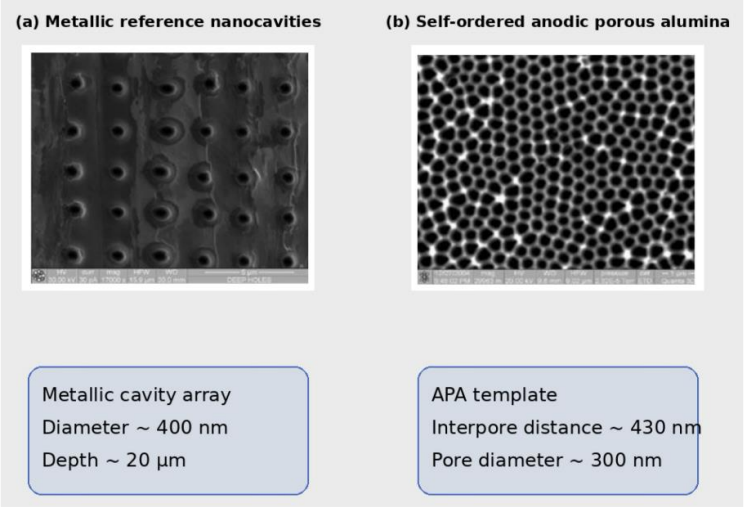

Figure 3. Experimental nanocavity platforms: (a) metallic cavity arrays, (b) self-ordered anodic porous alumina.

 doi:10.20944/preprints202605.0211.v1

Thus, the experimental archive establishes confinement-modified radiative behaviour in the accessible Vis/NIR window, whereas the mid-infrared mechanism discussed below is addressed through a targeted electromagnetic model rather than a direct experimental spectrum

4.2. Approximate Quantitative Indicators from Visible/NIR Spectra

To reduce purely verbal interpretation, approximate indicators were extracted by digitising the experimental curves in Figure 2. The comparison makes the trend explicit: smooth zirconia stays relatively close to the fitted grey-body curve, whereas Pt-coated APA shows a progressively stronger negative deviation toward the red edge of the measured window.

Table 2. Approximate figure-derived indicators extracted from the experimental spectra.

Sample	Pointwise deviation in measured window	Integrated 680-780 nm radiance / grey-body fit	Crossover behaviour	Interpretation
Smooth zirconia	+25% at 680 nm, +17% at 730 nm, +9% at 780 nm	≈ 1.15	No strong inversion relative to fit in the red tail	Reference remains comparatively close to grey-body behaviour within the experimental window.
Pt-coated APA	–15% at 660 nm, –34% at 730 nm, –45% at 780 nm	≈ 0.67	Experimental and fitted curves approach near 660-680 nm, then diverge strongly	Ordered Pt-coated nanocavity sample shows a much stronger long-wavelength depression in the measured window.

These indicators do not prove suppression in the unmeasured 2–15 μm band, but they do quantify the fact that the Pt-coated APA sample already departs from grey-body behaviour more strongly than zirconia in the preserved visible/NIR data.

4.3. Scope and Limitations

The present experimental dataset is limited in three ways: (i) only visible/NIR spectra are available; (ii) direct combustion metrics are missing; (iii) full replication metadata are not preserved. A targeted electromagnetic assessment of the cavity geometry is therefore introduced in Section 5. The manuscript is a mechanistically grounded concept paper built on experimental indication and targeted numerical assessment.

5. Targeted FDTD Assessment of Mid-Infrared Radiative-Channel Redistribution

5.1. What Was Measured Experimentally and What Was simulated

The experimental basis (Section 4) establishes two robust facts: (i) Pt-coated APA departs more strongly from grey-body behaviour than zirconia in the preserved visible/NIR window, and (ii) the relevant cavity dimensions are in the 300–400 nm range with high aspect ratio. The simulations address a different question. They do not reproduce combustion chemistry, species transport, catalytic conversion, or the full thermal field of the reactor. Instead, they probe the electromagnetic response of a representative emitting nanocavity in the mid-infrared, where the rovibrational bands of H_2O and CO_2 lie and where no archived spectra are available. In that sense, the numerical work is a **targeted electromagnetic surrogate**: it asks how a local emitter placed in a Pt-coated pore experiences the cavity-modified optical environment, and how much of the emitted power is retained in wall-coupled channels versus escaping through the pore apertures.

 doi:10.20944/preprints202605.0211.v1

5.2. Model Assumptions and Numerical Setup

A single cylindrical pore is simulated in cylindrical symmetry using the open-source MEEP finite-difference time-domain solver [39], with the converged benchmark evaluated at azimuthal order m = 0, exploiting rotational symmetry. The cavity is embedded in an Al_2O_3 matrix with refractive index n = 1.63 and lined by a conformal Pt coating of thickness t_{Pt} = 50 nm. The representative benchmark geometry uses nominal pore diameter D = 300 nm, cavity depth L = 20 μm, and lattice pitch a = 430 nm, consistent with the structural scale of the experimental APA platform. The effective free cavity diameter is $D_{eff} = D - 2\,t_{Pt}$ = 200 nm.

Platinum is described by a Drude dielectric function (ω_p = 9.59 eV, γ = 0.048 eV). A radially polarised point dipole is placed at the cavity mid-plane, at a radial distance of about 50 nm from the Pt wall. This source is an electromagnetic proxy for a local rovibrational emitter, not a full representation of combustion chemistry. For each wavelength, the local density of optical states is quantified through the Purcell factor F_P = LDOS_cav / LDOS_vac, obtained by comparing the cavity run with a matched vacuum reference. In addition to LDOS, monitor-based flux diagnostics record the total power crossing a closed box around the source region and the power passing through the cavity apertures.

Two numerical levels were used. First, an exploratory Phase-1 survey screened four diameters (250, 300, 350, 500 nm) across the 2.7, 4.3, 6.3 and 15.0 μm bands using lighter numerical settings intended only for rapid band selection. Those calculations identified the CO_2-4.3 μm band as the strongest case, but they are not treated here as converged quantitative results.
Second, a rigorous benchmark was carried out for the representative case D = 300 nm and λ = 4.3 μm with progressive refinement from 200 to 400 px/μm, PML thickness increased to 6 μm, decay threshold set to 10^{-6}, complex fields enabled, and epsilon averaging applied.

5.3. Results

The exploratory four-band survey served to identify the CO_2-4.3 μm band as the dominant candidate for detailed analysis; its higher preliminary values are not used here as converged quantitative benchmarks. The **converged benchmark** for the representative Pt-coated cavity provides the physically defendable result:

- The LDOS-based Purcell factor stabilises at $F_P \approx 1.26$ (≈ +26%) at 400 px/μm, with negligible change between 300 and 400 px/μm.
- The Au cross-check yields the same value within numerical precision (difference < 0.0001), confirming that the effect is purely geometric in the deep-Drude mid-infrared regime.
- Within the present monitor configuration, the box-integrated power enhancement is larger than the LDOS enhancement, while the recorded aperture power remains more than six orders of magnitude smaller than the box-integrated signal.

These numbers are summarised in **Table 3**.

Table 3. Converged FDTD results for the representative Pt-coated cavity (D = 300 nm, L = 20 μm, t_{Pt} = 50 nm, λ = 4.3 μm).

Quantity	Value	Interpretation
$LDOS_{vac}$ (reference)	634.0	Normalisation
$LDOS_{cav}$	801.2	Enhanced total LDOS
Purcell factor F_P (LDOS)	1.26	+26% total LDOS enhancement
Purcell factor F_P (box)	≈ 2.8	Additional redistribution into flux surfaces
Ratio P_{box} / $P_{aperture}$	> 10^6	Extreme suppression of free-space axial emission

These values are obtained from a fully converged simulation at 400 px/μm resolution.

Figure 4 presents the convergence plot and the power flow analysis. Panel (a) shows the asymptotic stabilisation of F_P towards 1.26 as resolution increases; the Au point at 400 px/μm overlaps

 doi:10.20944/preprints202605.0211.v1

the Pt benchmark. Panel (b) shows the large mismatch between box-integrated power (which includes wall-coupled energy) and aperture power (free-space escape), consistent with radiative-channel redistribution.

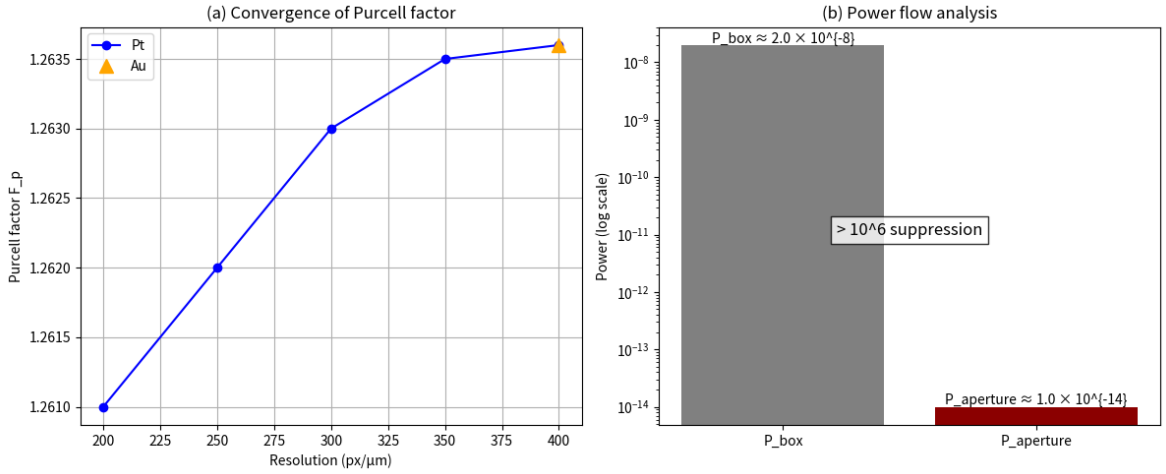

Figure 4. FDTD convergence and power-flow analysis for the representative Pt-coated nanocavity (D = 300 nm, λ = 4.3 μm). (a) Convergence of the LDOS-based Purcell factor with spatial resolution. The value stabilises at F_p ≈ 1.26; the Au cross-check at 400 px/μm overlaps the Pt result. (b) Comparison of box-integrated total radiated power versus power escaping through the cavity apertures (log scale). The ratio exceeds 10^6, demonstrating strong suppression of free-space axial escape.

5.4. Interpretation and Scientific Scope

The converged 4.3 μm benchmark refines the heuristic cutoff picture without overturning it. The idealised cutoff argument correctly predicts that *propagating transverse modes* are cut off, strongly suppressing free-space axial escape. However, a realistic open metallic cavity also supports evanescent fields, surface-plasmon-polariton modes and longitudinal resonances, all of which contribute to the total LDOS and can make $F_p > 1$. The monitor-based flux diagnostics then show that despite the enhanced total LDOS, only a negligible fraction of the emitted power leaves the cavity through the apertures. The majority is redirected into wall-coupled or non-axially escaping channels.

Therefore, the mechanism is not a blanket suppression of total LDOS, but a redistribution of radiative channels: the cavity enhances the total emission rate of a local source, while simultaneously channelling the emitted energy into the solid matrix (where it can be recovered as heat) rather than allowing it to radiate freely into space. This is precisely the regime required for a hybrid TPV/TEG system.

The simulations remain limited to a single-pore axisymmetric geometry and do not include array coupling or reactive-flow effects. They should be read as a targeted electromagnetic assessment anchored by a converged 4.3 μm benchmark

6. Relevance for Selective Energy Conversion

The most immediate selective-energy-conversion route is thermophotovoltaic (TPV) conversion. In conventional combustion-driven TPV systems, the burner and the selective-emission function are often separated conceptually or physically. The distinctive proposition here is different: the combustor itself is geometrically engineered as the selective emitter through catalytic nanocavities. This places the Pt-coated APA platform between classical porous catalysts and idealised cavity-optics emitters: it remains an open, lossy, array-coupled reactor, but one whose geometry can still bias the spectral branching of the emitted energy [20–26,34,35].

 doi:10.20944/preprints202605.0211.v1

The targeted FDTD benchmark of Section 5 indicates that, under the representative single-pore model, the converged benchmark at the CO_2-4.3 μm band shows moderate total LDOS enhancement ($F_P \approx 1.26$) together with extreme suppression of aperture escape. This is the optimal regime for a combined TPV/TEG system: the energy not radiated to the TPV cell is deposited as heat in the walls, where a thermoelectric generator can convert it into electricity. Figure 5 summarises the proposed energy-conversion logic.

Assumed suppression of the 2–15 μm relative band versus grey-body behaviour can be expressed through an emitter spectral-efficiency metric η_spec for a representative emitter temperature of 1700 K and a GaSb-like cutoff near 1.8 μm. The scenarios in Table 4 are illustrative first-order sensitivity estimates based on free-space escape, not on total LDOS.

Table 4. Illustrative TPV spectral-efficiency sensitivity for assumed long-wave suppression scenarios (based on free-space escape).

Assumed suppression of 2–15 μm relative band (radiative escape)	Relative TPV spectral efficiency vs. baseline	η_spec for $\lambda_g \approx 1.8$ μm
0%	1.00	0.29
10%	1.15	0.33
30%	1.23	0.36
50%	1.34	0.39

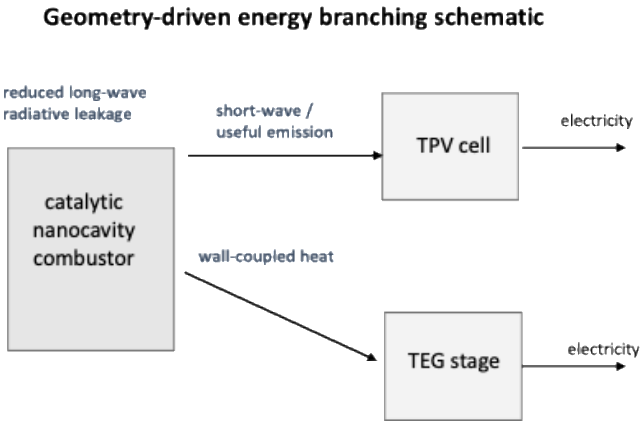

Figure 5. Schematic outline of confined combustion as a radiative-branching problem where the combustor behaves as a geometrically engineered selective emitter for TPV and a conductive branch for TEG.

7. Validation Roadmap Toward Selective Energy-Conversion Devices

A stringent evaluation of the nanocavity-selective-emission hypothesis should combine four coupled axes. First, spectral acquisition should be extended beyond the current visible/NIR window to the 2–15 μm thermal band, where the dominant rovibrational bands of H_2O and CO_2 occur. Second, cavity diameter, depth and Pt thickness should be varied systematically so that geometric control can be mapped directly onto spectral redistribution. Third, optical data should be acquired together with chemical and thermal diagnostics, including fuel conversion, ignition/extinction thresholds, local wall temperature, product composition, NO_x formation, catalyst stability and run-to-run repeatability. Fourth, the platform should be coupled to an actual downstream converter so that spectral selectivity can be compared with electrical output.

The targeted FDTD assessment of Section 5 provides a first quantitative step. A complementary extended modelling program would further sharpen the mechanism. Electromagnetic simulations of open, lossy, array-coupled pores, combined with simplified catalytic-reaction and radiative-transfer models, could determine whether the observed spectral deviations can be generated by measured pore geometry and wall properties, or whether additional contributions from Pt loss, localised

 doi:10.20944/preprints202605.0211.v1

catalytic heating and inter-cavity coupling must be invoked. In that form, theory becomes a discriminating test of the nanocavity-mediated interpretation rather than a generic add-on.

This validation roadmap is intentionally specific because the present manuscript aims to move from qualitative plausibility to quantitatively testable confined-combustion photonics and, ultimately, to experimentally validated selective energy conversion. The decisive outcome is whether geometry-controlled spectral redistribution remains visible once full-spectrum diagnostics, combustion metrics and model-based discrimination are brought onto the same platform.

8. Conclusions

Confined combustion is interpreted here as a bio-inspired, multiscale selective-energy-conversion problem in which catalytic interfaces, cavity geometry and radiative relaxation are co-designed rather than treated independently. The experimental visible/NIR data from Pt-coated anodic porous alumina provide direct experimental indication of confinement-modified radiative behaviour at accessible wavelengths. The idealised waveguide cutoff argument shows that free-space axial propagation is strongly suppressed for mid-infrared bands in pores of 300–400 nm diameter.

The targeted FDTD assessment (Section 5) refines this picture: in the representative single-pore benchmark at the CO_2-4.3 μm band, the total LDOS is moderately enhanced ($F_P \approx 1.26$), while the power escaping through the apertures is suppressed by more than six orders of magnitude relative to the total radiated power. This demonstrates a radiative-channel redistribution mechanism rather than a blanket suppression of total LDOS.

The central mechanistic proposal is deliberately limited and specific: for pore diameters of about 300–400 nm, long-wave rovibrational emission is placed in a strong geometric-disadvantage regime for free-space axial escape, so the radiative branching of combustion products can shift away from free infrared escape and toward wall coupling, quenching and structured heat recovery. This is a geometric LDOS-control picture under realistic combustion conditions, not a claim of strong coupling or of elimination of molecular internal states.

Within that scope, the manuscript contributes a single integrated viewpoint: catalytic microcombustion, nanocavity-mediated photonic control and confined chemistry can be interpreted within one photonic-chemical coupling framework for selective energy conversion. The immediate consequence is a plausible route toward combustor-integrated selective emitters for TPV and hybrid TPV/TEG conversion. The decisive next step is quantitative closure through full-spectrum measurement, coupled modelling and integrated energy-conversion tests.

Acknowledgments: This work was supported by HORIZON-JU-Chips-2025-1-IA NeAIxt grant no. 101194172, and by HORIZON-JU-Chips-2023-1-IA EdgeAI-Trust grant no. 101139892.

Acronyms

Acronym	Meaning	Acronym	Meaning
APA	Anodic Porous Alumina	NO_x	Nitrogen Oxides
FDTD	Finite-Difference Time-Domain	Pt	Platinum
IR	Infrared	RCWA	Rigorous Coupled-Wave Analysis
LDOS	Local Density of Optical States	TEG	Thermoelectric Generator
NIR	Near-Infrared	TPV	Thermophotovoltaic
PML	Perfectly Matched Layer	Vis/NIR	Visible/Near-Infrared

References

1. [1] Bykov VP. Spontaneous emission in a periodic structure. Sov Phys JETP. 1972;35(2):269-273.
2. [2] Yablonovitch E. Inhibited spontaneous emission in solid-state physics and electronics. Phys Rev Lett. 1987;58(20):2059-2062. doi:10.1103/PhysRevLett.58.2059

 doi:10.20944/preprints202605.0211.v1

3. [3] John S. Strong localization of photons in certain disordered dielectric superlattices. Phys Rev Lett. 1987;58(23):2486-2489. doi:10.1103/PhysRevLett.58.2486
4. [4] Chang RK, Campillo AJ, editors. Optical Processes in Microcavities. Singapore: World Scientific; 1996. doi:10.1142/2828
5. [5] Mitchell P. Coupling of phosphorylation to electron and hydrogen transfer by a chemiosmotic type of mechanism. Nature. 1961;191:144-148. doi:10.1038/191144a0
6. [6] Bar-Peled L, Kory N. Principles and functions of metabolic compartmentalization. Nat Metab. 2022;4(10):1232-1244. doi:10.1038/s42255-022-00645-2
7. [7] Flori S, Jouneau PH, Bailleul B, Gallet B, Estrozi LF, Schober A, et al. Plastid thylakoid architecture optimizes photosynthesis in diatoms. Nat Commun. 2017;8:15885. doi:10.1038/ncomms15885
8. [8] Trimmer BA, Aprille JR, Dudzinski DM, Lagace CJ, Lewis SM, Michel T, et al. Nitric oxide and the control of firefly flashing. Science. 2001;292(5526):2486-2488. doi:10.1126/science.1059833
9. [9] Kim JJ, Lee Y, Kim HG, Choi KJ, Kweon HS, Park S, Jeong KH. Biologically inspired LED lens from cuticular nanostructures of firefly lantern. Proc Natl Acad Sci U S A. 2012;109(46):18674-18678. doi:10.1073/pnas.1213331109
10. [10] Bay A, Cloetens P, Suhonen H, Vigneron JP. Improved light extraction in the bioluminescent lantern of a Photuris firefly (Lampyridae). Opt Express. 2013;21(1):764-780. doi:10.1364/OE.21.000764
11. [11] Hu HW, Carson GA, Granick S. Relaxation time of confined liquids under shear. Phys Rev Lett. 1991;66(21):2758-2761. doi:10.1103/PhysRevLett.66.2758
12. [12] Cui ST, McCabe C, Cummings PT, Cochran HD. Molecular dynamics study of the nanorheology of n-dodecane confined between planar surfaces. J Chem Phys. 2003;118(19):8941-8944. doi:10.1063/1.1568084
13. [13] Fernandez-Pello AC. Micropower generation using combustion: issues and approaches. Proc Combust Inst. 2002;29(1):883-899. doi:10.1016/S1540-7489(02)80113-4
14. [14] Ju Y, Maruta K. Microscale combustion: technology development and fundamental research. Prog Energy Combust Sci. 2011;37(6):669-715. doi:10.1016/j.pecs.2011.03.001
15. [15] Maruta K. Micro and mesoscale combustion. Proc Combust Inst. 2011;33(1):125-150. doi:10.1016/j.proci.2010.09.005
16. [16] Ahn J, Eastwood C, Sitzki L, Ronney PD. Gas-phase and catalytic combustion in heat-recirculating burners. Proc Combust Inst. 2005;30(2):2463-2472. doi:10.1016/j.proci.2004.08.265
17. [17] Pullini D, Repetto P, Bernard S, Doskolovich L, Perlo P. Rigorous calculations and fabrication by self-assembly techniques of 2D subwavelength structures of gold for photonic applications. Appl Opt. 2005;44(24):5127-5130. doi:10.1364/AO.44.005127
18. [18] Stura E, Bruzzese D, Valerio F, Grasso V, Perlo P, Nicolini C. Anodic porous alumina as mechanical stability enhancer for LDL-cholesterol sensitive electrodes. Biosens Bioelectron. 2007;23(5):655-660. doi:10.1016/j.bios.2007.07.011
19. [19] Gordon IE, Rothman LS, Hill C, Kochanov RV, Tan Y, Bernath PF, et al. The HITRAN2016 molecular spectroscopic database. J Quant Spectrosc Radiat Transfer. 2017;203:3-69. doi:10.1016/j.jqsrt.2017.06.038
20. [20] Li W, Fan S. Nanophotonic control of thermal radiation for energy applications [Invited]. Opt Express. 2018;26(12):15995-16021. doi:10.1364/OE.26.015995
21. [21] Baranov DG, Xiao Y, Nechepurenko IA, Krasnok A, Alù A, Kats MA. Nanophotonic engineering of far-field thermal emitters. Nat Mater. 2019;18(9):920-930. doi:10.1038/s41563-019-0363-y
22. [22] Gentillon P, Singh S, Lakshman S, Lanzini A, Santarelli M, Torchio MF. A comprehensive experimental characterisation of a novel porous media combustion-based thermophotovoltaic system with controlled emission. Appl Energy. 2019;254:113721. doi:10.1016/j.apenergy.2019.113721
23. [23] Sakakibara R, Stelmakh V, Chan WR, Ghebrebrhan M, Joannopoulos JD, Soljačić M, Čelanović I. Practical emitters for thermophotovoltaics: a review. J Photonics Energy. 2019;9(3):032713. doi:10.1117/1.JPE.9.032713
24. [24] Qian Z, Shan L, Zhang X, Liu Q, Ma Y, Gong Q. Spontaneous emission in micro- or nanophotonic structures. PhotoniX. 2021;2:21. doi:10.1186/s43074-021-00043-z
25. [25] LaPotin A, Schulte KL, Steiner MA, Buznitsky K, Kelsall CC, Friedman DJ, et al. Thermophotovoltaic efficiency of 40%. Nature. 2022;604(7905):287-291. doi:10.1038/s41586-022-04473-y

 doi:10.20944/preprints202605.0211.v1

26. [26] Chen S, Guo Y, Pan Q, Shuai Y. A review on current development of thermophotovoltaic technology in heat recovery. Int J Extrem Manuf. 2024;6(2):022009. doi:10.1088/2631-7990/ad1dca
27. [27] Federici JA, Norton DG, Bruggemann T, Voit KW, Wetzel ED, Vlachos DG. Catalytic microcombustors with integrated thermoelectric elements for portable power production. J Power Sources. 2006;161(2):1469-1478. doi:10.1016/j.jpowsour.2006.06.042
28. [28] Ismail AK, Abdullah MZ, Zubair M, Ahmad ZA, Jamaludin AR, Mustafa KF, Abdullah MN. Application of porous medium burner with micro cogeneration system. Energy. 2013;50:131-142. doi:10.1016/j.energy.2012.12.007
29. [29] Grommet AB, Feller M, Klajn R. Chemical reactivity under nanoconfinement. Nat Nanotechnol. 2020;15(4):256-271. doi:10.1038/s41565-020-0652-2
30. [30] Dong B, Pei Y, Mansour N, Lu X, Yang K, Huang W, Fang N. Deciphering nanoconfinement effects on molecular orientation and reaction intermediate by single molecule imaging. Nat Commun. 2019;10:4815. doi:10.1038/s41467-019-12799-x
31. [31] McCormack KL, Li J, Yoklavich TJ, Xia Y. A review of fluids under nanoconfinement: Reactivity, geomechanics, phase transitions, and flow. Phys Fluids. 2024;36(9):091301. doi:10.1063/5.0224861
32. [32] Wang M, Zhou C, Akter N, Tysoe WT, Boscoboinik JA, Lu D. Mechanism of the accelerated water formation reaction under interfacial confinement. ACS Catal. 2020;10(11):6119-6128. doi:10.1021/acscatal.9b05289
33. [33] Yao K, Kong G, Zhang D, Zhou H, Zheng Y. Bioinspired photonic materials for advanced thermal management. Chem Soc Rev. 2025. doi:10.1039/D5CS00471C
34. [34] Zhang Y, Tian Q, Zheng S, Yan M, Zhang M. Coherent control of thermal radiation with nanophotonics. Adv Photonics Res. 2025;6(10):2500019. doi:10.1002/adpr.202500019
35. [35] Wang H, Xu Z, Wang C, Hou Z, Bian M, Zhuang N, Tao H, Wang Y, Tang X. Optimized design and application performance analysis of heat recovery hybrid system for radioisotope thermophotovoltaic based on thermoelectric heat dissipation. Appl Energy. 2024;355:122259. doi:10.1016/j.apenergy.2023.122259
36. [36] Itoh H, Yanagishita T. Anodic porous alumina membranes with chemical stability improved by atomic layer deposition coating of TiO_2. ECS J Solid State Sci Technol. 2024;13:023002. doi:10.1149/2162-8777/ad2197
37. [37] Roelli P, Hu H, Verhagen E, Reich S. Nanocavities for molecular optomechanics: their fundamental description and applications. ACS Photonics. 2024;11(11):4486-4501. doi:10.1021/acsphotonics.4c01548
38. [38] Garner SM, Li X, Hammes-Schiffer S. Simulation of vibronic strong coupling and cavity-modified hydrogen tunneling dynamics. J Chem Phys. 2025;163(13):134113. doi:10.1063/5.0286132
39. [39] Oskooi AF, Roundy D, Ibanescu M, Bermel P, Joannopoulos JD, Johnson SG. Meep: a flexible free-software package for electromagnetic simulations by the FDTD method. Comput Phys Commun. 2010;181(3):687-702. doi:10.1016/j.cpc.2009.11.026